Strength of Shock-Loaded Single-Crystal Tantalum [100] Determined using *In Situ* Broadband X-Ray Laue Diffraction

A. J. Comley,[1,2] B. R. Maddox,[1] R. E. Rudd,[1] S. T. Prisbrey,[1] J. A. Hawreliak,[1] D. A. Orlikowski,[1] S. C. Peterson,[1] J. H. Satcher,[1] A. J. Elsholz,[1] H.-S. Park,[1] B. A. Remington,[1] N. Bazin,[2] J. M. Foster,[2] P. Graham,[2] N. Park,[2] P. A. Rosen,[2] S. R. Rothman,[2] A. Higginbotham,[3] M. Suggit,[3] and J. S. Wark[3]

[1]*Lawrence Livermore National Laboratory, Livermore, California 94550, USA*

[2]*Atomic Weapons Establishment, Aldermaston, Reading RG7 4PR, United Kingdom*

[3]*Department of Physics, Clarendon Laboratory, University of Oxford, Parks Road, Oxford OX1 3PU, United Kingdom*

(Received 2 July 2012; published 11 March 2013)

The strength of shock-loaded single crystal tantalum [100] has been experimentally determined using *in situ* broadband x-ray Laue diffraction to measure the strain state of the compressed crystal, and elastic constants calculated from first principles. The inferred strength reaches 35 GPa at a shock pressure of 181 GPa and is in excellent agreement with a multiscale strength model [N. R. Barton *et al.*, J. Appl. Phys. **109**, 073501 (2011)], which employs a hierarchy of simulation methods over a range of length scales to calculate strength from first principles.

DOI: 10.1103/PhysRevLett.110.115501 PACS numbers: 62.20.F−, 61.05.cp, 62.50.Ef

The response of materials to dynamic compressive loading has been the subject of intense research over recent years [1]. It is well known that when a material is subjected to a shear stress in excess of the elastic limit during uniaxial compression, plastic relaxation processes act to reduce that stress until its ultimate limiting value, the material strength, is reached. Strength causes solids to deviate from idealized fluidlike response, and is important for a full understanding of wave propagation, compression, and hydrodynamic instability evolution in metals [2].

Strength is a complex function of material parameters and loading conditions (pressure and strain rate) and is often treated with the use of empirical constitutive models [3]. While these models are useful, a true understanding of strength requires a theoretical framework based on first principles that can make reliable predictions over a wide range of pressures and strain rates, and suitable experimental techniques to validate those predictions.

In situ x-ray diffraction is a powerful experimental technique for characterizing the state of shock-compressed material, because it yields direct experimental information on crystal strain as a function of applied loading (pressure), from which strength can be inferred. For example, recent experiments have inferred the strength in shock-compressed Cu [4], Fe [5], and Al [6]. However, there are few such data available for high-Z elements. This is because as the atomic number of the sample increases, the technique becomes more challenging; very bright sources of increasingly higher energy x rays are required to probe the high-density region of the compressed sample [7]. In this Letter, we report on the first measurements of strain and associated strength of Ta single crystals shocked along the [100] direction at shock stresses up to ~205 GPa, and show that the results compare favorably with a strength model calculated from first principles.

The experimental technique used was broadband (''white-light'') x-ray diffraction in transmission Laue geometry [8,9]. This method was enabled by an implosion capsule x-ray source [10] that produced a broadband, smoothly varying, and repeatable bremsstrahlung spectrum with photon energies up to ~25 keV and a typical implosion emission time scale of ~150 ps, which set the temporal resolution of the x-ray diffraction probe. The capsule provides a convenient means of converting a large amount of laser energy (> 20 kJ) into a high-energy x-ray ''point'' source suitable for probing high-Z materials such as Ta.

In this white-light x-ray diffraction technique, multiple crystallographic planes in the sample satisfy the Bragg condition simultaneously, each such plane giving rise to a characteristic spot in the resulting diffraction pattern (Fig. 1). The Laue spots are formed by the quasicollimating effect of a pinhole on which the sample is mounted; the locations of the spots on the detectors are sensitive to the strain state of the sample, as discussed later.

Figure 1 also shows the experimental geometry. The implosion capsule x-ray source was placed 20 mm from the surface of the sample. Diffracted x rays were recorded on image plate detectors [11] mounted on the inside of a pyramid-shaped enclosure made of tungsten alloy (heavimet), referred to as the broadband x-ray diffraction (BBXRD) diagnostic, which also served to mount the sample during the experiment. Each sample consisted of a 5 μm-thick tantalum crystal embedded between a 10 μm-thick nanocrystalline, high-density carbon (n-HDC) ablator and a 40 μm-thick optically transparent microcrystalline HDC (μ-HDC) tamper. Epoxy layers at the HDC-Ta interfaces were 2 ± 1 μm thick, and each crystal package was mounted on a heavimet collimating pinhole with a nominal aperture diameter of 250 μm.

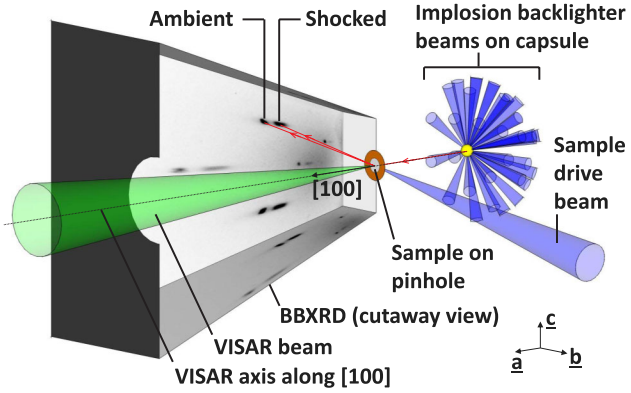

FIG. 1 (color online). Experimental geometry. The crystal sample is mounted on a pinhole on the front of the BBXRD diagnostic, and is shock-loaded along the [100] direction using a single beam of the OMEGA laser system. The sample drive beam is incident at an angle of 24.8° to the surface normal, and the VISAR axis is aligned along [100]. Continuum (white light) x rays from a prompt capsule implosion driven by 44 beams are collimated by the pinhole and diffracted from the sample to produce a characteristic Laue diffraction pattern on image plate detectors mounted on the interior of the BBXRD enclosure (example rays are shown in red). Each diffraction spot is attributable to a particular crystallographic plane and is formed by the quasicollimating effect of the pinhole on which the crystal sample is mounted.

A shock was launched perpendicular to the ablator surface into the sample by a single beam of the OMEGA laser system, which was incident at an angle of 24.8° to the ablator surface normal. The tantalum crystal orientation was chosen such that the shock propagated along the [100] direction of the crystal. The drive laser had a 1 ns square pulse shape, energy between 10 and 45 J (at laser wavelength of 351 nm), and was focused using an SG8 distributed phase plate which generates a super-Gaussian flat-top spot with a $1/e$ radius of 438 μm. The capsule backlighter was driven by 44 beams, each with nominally 500 J at 351 nm in a 1 ns square pulse, focused using an SG4 distributed phase plate to a spot with a $1/e$ radius of 352 μm. Simultaneously, VISAR was used to measure the velocity of the interface between the Ta and the μ-HDC tamper.

The peak applied longitudinal stress σ_S experienced by the Ta sample was calculated using a standard impedance-matching method [12] applied at both the ablator-Ta and Ta-tamper interfaces, with the assumption that the epoxy layers can be ignored (the validity of which is discussed below), and using Hugoniot data from Ref. [13] (ablator and tamper) and Ref. [14] (Ta). Additionally, the analysis of the ablator-Ta interface requires the longitudinal stress developed in the ablator σ_{HDC}, which was calculated from the scaling law $\sigma_{\mathrm{HDC}}(\mathrm{GPa}) = 42I(\mathrm{TW/cm^2})^{0.71}$ [15], where I is the laser drive intensity. In the analysis of the Ta-tamper interface, the peak velocity of that interface was used, and was obtained by taking the peak apparent velocity measured using VISAR and dividing it by a window correction factor of 2.7, appropriate for the μ-HDC tamper which also acted as a velocimetry window. The correction factor was determined from the linear relationship between the refractive index and density for diamond [16].

The results from the two impedance-matching calculations were averaged to produce the quoted value for σ_S and associated error bars. Detailed simulations of the shock propagation through the target package show that when the glue layers are taken into account, the range of stress states in the compressed crystal at the time of the x-ray diffraction measurement is encompassed by the error bars resulting from the impedance matching analysis. In essence, shock reverberations in the epoxy layer between the ablator and Ta sample are observed in the simulations as the epoxy "rings up" to peak pressure, but are seen to coalesce promptly in the Ta to produce a well-defined compressed region, consistent with the observations as described below.

Figure 2 shows representative diffraction patterns recorded on a single image plate of the BBXRD diagnostic at two different shock stresses. Because of symmetry in the experimental geometry (the capsule being placed on the BBXRD axis as shown in Fig. 1), the pattern is repeated on the other three image plates mounted orthogonally with respect to one another in the interior of the diagnostic enclosure.

In these experiments we probe the Ta sample (pulse the white-light backlighter) when the shock has traversed part of the way through the sample. We therefore record the superposition of two distinct diffraction patterns: one from the ambient crystal which serves as a zero-compression reference pattern, and one from the compressed crystal,

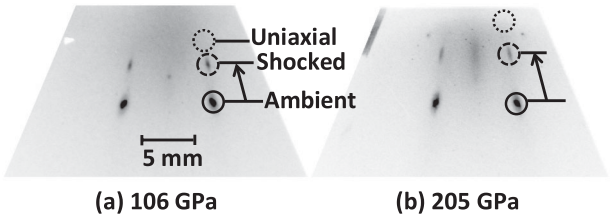

FIG. 2. (a) Diffraction pattern recorded from a partially shocked Ta [100] sample at a longitudinal stress of 106 GPa, illustrating features with Miller indices (211) attributable to both the ambient (solid circle) and shocked (dashed circle) sections of the crystal sample. The dotted circles indicate the approximate location of a diffraction spot that would be produced by a uniaxially compressed crystal at that longitudinal stress. The black arrows indicate the direction in which the dashed-circled spots shift with increasing strain. (b) Diffraction pattern annotated as in (a) but at a longitudinal stress of 205 GPa. Note the black arrow is longer than the corresponding arrow in (a), representative of an increase in the crystal strain at the higher longitudinal stress.

which is spatially shifted with respect to the ambient pattern on the detector.

This shift is a function of the aspect ratio α of the compressed unit cell, defined as $\alpha = |\underline{\boldsymbol{a}}|/|\underline{\boldsymbol{b}}| = |\underline{\boldsymbol{a}}|/|\underline{\boldsymbol{c}}| = (1-\varepsilon_S)/(1-\varepsilon_T)$, where $\underline{\boldsymbol{a}}$, $\underline{\boldsymbol{b}}$, and $\underline{\boldsymbol{c}}$ are the unit cell vectors and ε_S and ε_T are the strains in the shock and transverse directions, respectively (here $\underline{\boldsymbol{a}}$ is aligned with the direction of shock propagation). The strains are given by $\varepsilon_S = 1-(\alpha^2/\eta)^{1/3}$ and $\varepsilon_T = 1-(\alpha\eta)^{-1/3}$, where $\eta = \rho_m/\rho_{m0}$ is the compression and ρ_m and ρ_{m0} are the compressed and initial mass density, respectively. We also define a shear strain as $\Delta\epsilon(\alpha,\eta) = \epsilon_S - \epsilon_T$.

In order to determine α from each diffraction pattern, ray tracing of the known experimental geometry from the x-ray source through to the detector, with application of Bragg's law at the sample, is employed to fit the diffraction pattern (on all four image plates) associated with the ambient crystal. This permits the diffraction spots in the pattern to be identified in terms of Miller indices, and the precise mounting orientation of the Ta sample to be determined. With the sample orientation known, the diffraction pattern of the compressed crystal is then fit using α as a single fitting parameter.

With the longitudinal stress σ_S and aspect ratio α determined for each shot, we proceed to calculate the pressure (mean stress) and strain state of the compressed crystal. Starting with the general tensor relation between stress and strain $\sigma_i = C_{ij}\varepsilon_j$, where C_{ij} are pressure-dependent single-crystal elastic constants in Voigt notation and due to cubic symmetry in the Ta lattice, only C_{11}, C_{12}, and C_{44} are nonzero. We denote $\sigma_1 = \sigma_S$ and $\sigma_2 = \sigma_3 = \sigma_T$, where σ_S and σ_T are the longitudinal and transverse stresses, respectively, and pressure $\bar{P} = (\sigma_S + 2\sigma_T)/3$. The stress-strain relation reduces to

$$\sigma_S = \sigma_S' + \bar{P}, \qquad \sigma_S' = \frac{4}{3}C'(\bar{P})\Delta\varepsilon(\alpha,\eta), \tag{1}$$

where σ_S' is the longitudinal deviatoric stress and $C'(\bar{P}) = [C_{11}(\bar{P}) - C_{12}(\bar{P})]/2$ is the effective shear modulus. We assume that the compressed state lies on the Ta Hugoniot, so that the compression η is a known function of $\bar{P}$ [14]. The shear modulus $C'(\bar{P})$ is calculated from density functional theory [17] (again assuming the compressed state is on the Hugoniot) and is shown in the inset to Fig. 4. The pressure is then obtained by solving Eq. (1) and the full strain state of the crystal can then be determined. The experimentally deduced shear strain $\Delta\varepsilon$ is shown as a function of applied stress in Fig. 3.

The data are compared with a uniaxial (1D) compression curve calculated using Eq. (1) with $\varepsilon_T = 0$. Purely hydrostatic compression would lie on the $\Delta\varepsilon = 0$ line. The observed strain is lower than that for uniaxial compression, indicating that the crystal has relaxed due to the onset of plastic flow. Over the time scale of the experiment ($\sim$1 ns, approximately the time taken for the shock to traverse the sample) we observe no difference in strain as a function of time within the experimental error bars for a given shock stress. Furthermore, there is no evidence of a partially relaxed region in the sample which would give rise to diffracted intensity in the region between the spots from the compressed crystal and the expected location of spots due to a uniaxially compressed crystal, as shown in Fig. 2.

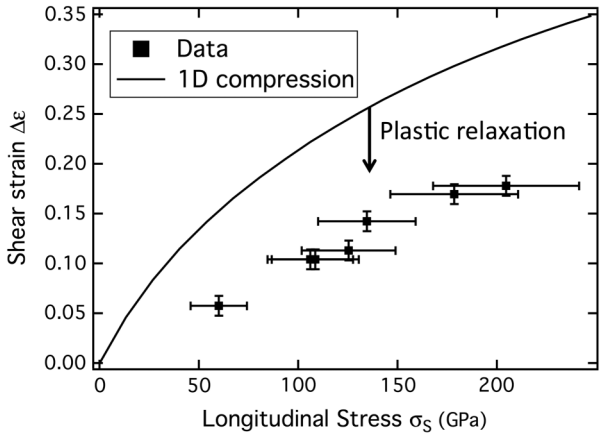

FIG. 3. Plot of shear strain $\Delta\varepsilon$ vs applied longitudinal stress σ_S. The measured strain is well below the calculated curve for 1D elastic compression, indicating plastic relaxation. Purely hydrostatic compression would lie on the $\Delta\varepsilon = 0$ line, corresponding to zero shear strain.

We therefore conclude that the material has reached a steady state and nonhydrostatic condition, such that the measured residual strain is related to the strength of the material, and that the relaxation to that state is much shorter than 1 ns. This conclusion is supported by molecular dynamics simulations [18] which indicate rapid (<5 ps) relaxation time scales above shock pressures of $\sim$60 GPa, due to the onset of homogenous nucleation and flow of dislocations which constitute the relaxation process. The von Mises strength $\bar{\sigma}$ is then readily calculated from $\bar{\sigma} = \frac{3}{2}\sigma_S' = 2C'(\bar{P})\Delta\varepsilon$, and is shown in Fig. 4 along with the strength predicted by a variety of models described in the literature.

In order to evaluate the strength models, the equivalent plastic strain $\bar{\varepsilon} = 2\Delta\varepsilon/3$ and strain rate $\dot{\varepsilon}$ are required. To estimate strain rate, we use the well-known Swegle-Grady relation $\dot{\varepsilon} = k\sigma_S^4$ [19], where $k = 27.34\ \mathrm{s^{-1}\,GPa^{-4}}$ for Ta [20]. This relation is valid when the Bland number $B = L/\delta \geq 1$ [21], where L is the sample thickness and $\delta = \frac{8}{3}C_0/(S\dot{\varepsilon})$ is the characteristic distance over which a step input wave would become steady. The parameters $C_0 = 3.414\ \mu\mathrm{m/ns}$ and $S = 1.2$ applicable to Ta [14] specify the equation of state relation $u_S = C_0 + Su_p$, where u_S and u_p are shock and particle speeds, respectively. For $\sigma_S = 130$ GPa (corresponding to approximately the center of the stress range in the data set), the Swegle-Grady relation gives $\dot{\varepsilon} = 7.8\times10^9\ \mathrm{s^{-1}}$, and

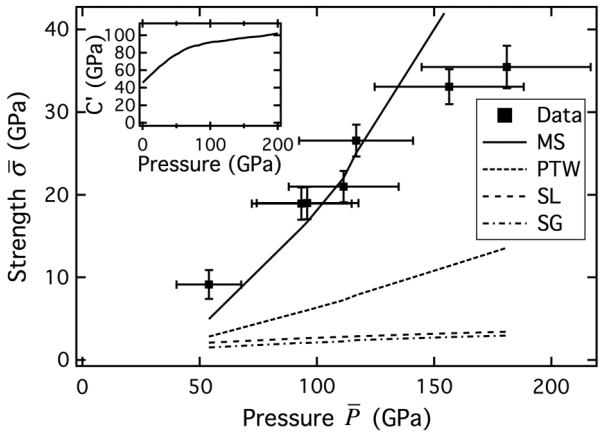

FIG. 4. Von Mises strength $\bar{\sigma}$ vs. pressure $\bar{P}$ as determined from the experiment, in comparison to strength predicted by the Steinberg-Guinan (SG) [19], Steinberg-Lund (SL) [20], Preston-Tonks-Wallace (PTW) [21], and the LLNL multiscale (MS) strength models [23]. Inset: effective shear modulus C' vs pressure $\bar{P}$, as calculated from density-functional theory including shock heating on the Hugoniot [14].

$\delta = 1$ μm. The Bland condition then demands that $L > 1$ μm to ensure that $B > 1$. For the current case $L = 5$ μm, we therefore assume that the Swegle-Grady relation provides a simple first-order estimate of the strain rate for the purpose of evaluating the strain rate dependent strength models.

Returning to Fig. 4, the Steinberg-Guinan (SG) [22] and Steinberg-Lund (SL) [23] models may not be expected to be applicable in the regime explored here, which represents a large extrapolation from where the models are known to be reliable. Indeed, we find that these models underpredict the strength by an order of magnitude. In the high strain rate regime of the experiment, the Preston-Tonks-Wallace (PTW) model [24] reduces to the power-law form $\bar{\sigma} \sim (\dot{\varepsilon}/\dot{\xi})^{0.23}$, where $\dot{\xi} = [\rho^{1/6} G(\bar{P}, T)]^{1/2}$, consistent with Wallace's theory of overdriven shocks in metals [25]. Here $G(\bar{P}, T)$ is the shear modulus (T being temperature) and was taken to be of the Steinberg-Guinan form. Although Wallace's theory is expected to be reliable to pressures >100 GPa [25], the strength predicted by the PTW model is a factor of ~3.3 lower than that obtained from the present experiment but does correctly reproduce the observed trend of higher strength with increasing pressure and strain rate.

To better understand the observed strength scaling we use a multiscale (MS) strength model described in Barton *et al.* [26], which employs a hierarchy of simulation methods starting from density functional theory and then passing information up through the scales, to calculate strength on the continuum level. Strength is obtained from the dislocation mobility law

$$\bar{\sigma} = M[\tau^*(v)\tau_P + \beta b G \rho_{\mathrm{sat0}}^{1/2} [\dot{\varepsilon}(\sigma_S)/\dot{\varepsilon}_0]^{n/2} + \tau_a], \quad (2)$$

where $M = 2.4495$ is the Taylor factor for ⟨100⟩ Ta, τ_P is the Peierls stress, b is the magnitude of the Burgers vector and $\tau^*(v)$ is a function of the mean dislocation velocity v that describes the drag and activation regimes of dislocation flow. The material parameters β, ρ_{sat0}, $\dot{\varepsilon}_0$, n, and τ_a are taken from Ref. [26].

We use a simplified form of the MS model in which the dislocation density is set equal to the saturation density $\rho_{\mathrm{sat}}(\dot{\varepsilon})$. This modification of the MS model is motivated by the molecular dynamics prediction of rapid dislocation nucleation at these high stresses, and the <5 ps nucleation period is treated as instantaneous. The MS model as published predicts slower dislocation multiplication and stress relaxation over a few ns [18], which is inconsistent with the experimental data. We also note that in the paper of Barton *et al.*, the shear modulus G for Ta reduces to the Steinberg-Guinan form, but with the exclusion of the thermal softening term. This was appropriate for successfully modeling low temperature Rayleigh-Taylor instability experiments [2,23]. However, in the case presented here, where the temperature is significant due to shock heating (temperatures of 650 to 4800 K for the range of shock pressures studied), we use the shear modulus calculated by Orlikowski *et al.* [17] to properly capture the effect of thermal softening. Excellent agreement with the data is obtained. At $\bar{P} = 100$ GPa ($\sigma_S \sim 113$ GPa) and $\dot{\varepsilon} = 4.5 \times 10^9$ s^{-1}, we find $\bar{\sigma}$18 GPa. For comparison, in the experiments of Park *et al.* [2], where rippled Ta samples were ramp-loaded to ~100 GPa and $\dot{\varepsilon}10^7$ s^{-1} to study Rayleigh-Taylor growth, the time-averaged flow stress in the evolving sample was ~6 GPa, namely, a factor ~3 lower. Both the results presented here and those of Park *et al.* were found to be consistent with the multiscale model and illustrate its ability to predict strength at high pressure over several orders of magnitude in strain rate.

This work was performed under the auspices of the U.S. Department of Energy by Lawrence Livermore National Security, LLC, Lawrence Livermore National Laboratory under Contract No. DE-AC52-07NA27344.

[1] M. A. Meyers, *Dynamic Behavior of Materials* (John Wiley & Sons, New York, 1994).
[2] H.-S. Park *et al.* (to be published).
[3] B. A. Remington *et al.*, Mater. Sci. Technol. **22**, 474 (2006).
[4] W. J. Murphy *et al.*, J. Phys. Condens. Matter **22**, 065404 (2010).
[5] J. A. Hawreliak *et al.*, Phys. Rev. B **83**, 144114 (2011).
[6] S. J. Turneaure and Y. M. Gupta, J. Appl. Phys. **109**, 123510 (2011).
[7] B. R. Maddox *et al.* (to be published).
[8] B. D. Cullity, *Elements of X-Ray Diffraction* (Addison-Wesley, Reading, 1978).
[9] M. Suggit, G. Kimminau, J. Hawreliak, B. Remington, N. Park, and J. Wark, Rev. Sci. Instrum. **81**, 083902 (2010).

[10] B. R. Maddox *et al.*, Phys. Plasmas **18**, 056709 (2011).
[11] B. R. Maddox, H. S. Park, B. A. Remington, N. Izumi, S. Chen, C. Chen, G. Kimminau, Z. Ali, M. J. Haugh, and Q. Ma, Rev. Sci. Instrum. **82**, 023111 (2011).
[12] Y. B. Zel'dovich and Y. P. Raizer, *Physics of Shock Waves and High-Temperature Hydrodynamic Phenomena* (Dover, Mineola, 2002).
[13] D. G. Hicks, T. R. Boehly, P. M. Celliers, D. K. Bradley, J. H. Eggert, R. S. McWilliams, R. Jeanloz, and G. W. Collins, Phys. Rev. B **78**, 174102 (2008).
[14] Y. Horie, L. Davison, and N. N. Thadani, *High Pressure Shock Compression of Solids VI* (Springer-Verlag, New York, 2003).
[15] D. E. Fratanduono, T. R. Boehly, P. M. Celliers, M. A. Barrios, J. H. Eggert, R. F. Smith, D. G. Hicks, G. W. Collins, and D. D. Meyerhofer, J. Appl. Phys. **110**, 073110 (2011).
[16] A. L. Ruoff and K. Ghandehari, AIP Conf. Proc. **309**, 1523 (1994); N. M. Balzaretti and J. A. H. da Jornada, Solid State Commun. **99**, 943 (1996).
[17] D. Orlikowski, P. Soderlind, and J. A. Moriarty, Phys. Rev. B **74**, 054109 (2006).
[18] R. E. Rudd, A. J. Comley, J. Hawreliak, B. Maddox, H.-S. Park, and B. A. Remington, AIP Conf. Proc. **1426**, 1379 (2012).
[19] J. W. Swegle and D. E. Grady, J. Appl. Phys. **58**, 692 (1985).
[20] L. E. Murr, M. A. Meyers, C.-S. Niou, Y. J. Chenz, S. Pappu, and C. Kennedy, Acta Mater. **45**, 157 (1997).
[21] D. R. Bland, IMA J. Appl. Math. **1**, 56 (1965).
[22] D. J. Steinberg, S. G. Cochran, and M. W. Guinan, J. Appl. Phys. **51**, 1498 (1980).
[23] D. J. Steinberg and C. M. Lund, J. Appl. Phys. **65**, 1528 (1989).
[24] D. L. Preston, D. L. Tonks, and D. C. Wallace, J. Appl. Phys. **93**, 211 (2003).
[25] D. C. Wallace, Phys. Rev. B **24**, 5597 (1981); D. C. Wallace, Phys. Rev. B **24**, 5607 (1981).
[26] N. R. Barton, J. V. Bernier, R. Becker, A. Arsenlis, R. Cavallo, J. Marian, M. Rhee, H.-S. Park, B. A. Remington, and R. T. Olson, J. Appl. Phys. **109**, 073501 (2011).